Wind and Structures, *Vol. 19, No. 2 (2014) 113-144*
DOI: http://dx.doi.org/10.12989/was.2014.19.2.113

Improvement and validation of a flow model for conical vortices

Jihong Ye[*1] and Xin Dong[1,2a]

[1]*Key laboratory for RC&PC Structures of China Ministry of Education, Southeast University, Nanjing 210096, China*
[2]*Tongji Architectural Design (Group) Co. Ltd, Shanghai 200092, China*

(Received June 19, 2013, Revised March 20, 2014, Accepted May 19, 2014)

Abstract. Separation bubble and conical vortices on a large-span flat roof were observed in this study through the use of flow visualization. The results indicated that separation bubble occurred when the flow was normal to the leading edge of the flat roof. Conical vortices that occur under the cornering flow were observed near the leading edge, and their appearance was influenced by the wind angle. When the wind changed from along the diagonal to deviating from the diagonal of the roof, the conical vortex close to the approaching flow changed from circular to be more oblong shaped. Based on the measured velocities in the conical vortices by flow visualization, a proposed two-dimensional vortex model was improved and validated by simplifying the velocity profile between the vortex and the potential flow region. Through measured velocities and parameters of vortices, the intensities of conical vortices and separation bubble on a large-span flat roof under different wind directions were provided. The quasi-steady theory was corrected by including the effect of vortices. With this improved two-dimensional vortex model and the corrected quasi-steady theory, the mean and peak suction beneath the cores of the conical vortices and separation bubble can be predicted, and these were verified by measured pressures on a larger-scale model of the flat roof.

Keywords: conical vortices; separation bubble; flat roof; flow model of vortex; prediction of suction beneath vortex cores; PIV experiment

1. Introduction

Two types of damaging vortices, known as separation bubbles and conical vortices, are well-known for their destructive effect on large-span roofs. The worst suction from these damaging vortices is generated at the leading edges and windward corners of the roofs. Suction induced by conical vortices is larger and more destructive than that of separation bubbles because the vorticity in separation bubble attenuates downstream. However, conical vortices have a velocity component along the leading edge that balances the dissipation of the vorticity. Therefore, conical vortices are stable and continuous, and the induced suction is more intense. Many studies have described examples of serious damage from suction induced by conical vortices (Kawai and Nishimura 1996, Lin *et al.* 1995). This suction falls beyond the provisions and predictions stated

∗Corresponding author, Professor, E-mail: yejihong@seu.edu.cn
[a] Doctoral candidate

http://www.techno-press.org/?journal=was&subpage=8 ISSN: 1226-6116 (Print), 1598-6225 (Online)

by wind-resistant design codes and traditional theories of wind engineering, and model-scale experiments in wind tunnels cannot adequately simulate the larger suctions beneath conical vortices. Tieleman (1996) pointed out that less satisfactory model and full-scale agreement exists between the fluctuating pressures in separation and reattachment regions. Theoretical numerical models, such as the Gaussian model, can be used for prediction only in a few particular cases because of the complexity of wind-structure aerodynamic interactions generated by the "blunt form" of structures (Gioffre and Grigoriu, 2001). Banks (2000) wrote that the quasi-steady theory ignores the contribution to peak suction by random vortex motion and random changes in vortex strength.

To control and predict the peak suction at the leading edges and corners of the roof, current research projects have investigated the mechanism by which the conical vortices induced suction on roofs. Marwood and Wood (1997) conducted simultaneous pressure-velocity measurements to assess the effect of instantaneous conical vortex position on roof suction. The results indicated that the position of the conical vortex varied significantly, and fluctuation pressures on the roof are closely linked to this variation. The peak suction is always located beneath the vortex cores. Wu *et al.* (2001) revealed that the horizontal wind angle predominantly determines the formation and configuration of conical vortices. The vertical wind angle modifies the configuration and movement of conical vortices, and sporadically large and fast excursions of the vertical angle can significantly change the configuration of vortices and subsequently generate extremely high suction on roofs. Kawai (2002) found that when large-scale gust attacks a building instantly from a particular direction in any mean wind direction, peak suction is induced by the vortices. Synchronized measurements of the incident wind and the pressure were conducted by Zhao at Texas Tech University (TTU) (Zhao 1997). The results showed that the instantaneous peak suction beneath conical vortices is related to the instantaneous gust with a magnitude larger than the mean velocity. However, most studies explain the cause of larger suction from a qualitative point of view. To control the larger suction induced by vortices, the mechanism by which the vortex induced suction on roofs and the quantitative relationship between the upstream flow, the vortex and the roof suction should be given. Some exploratory research has been carried out on this issue. Kawai (1997) clarified the structure of conical vortices through velocity measurement with a hot-wire probe, implying that the lateral component of the approaching turbulence amplifies the sway of the vortices and induces much greater fluctuation in suction on the roof. Based on a Rankine vortex, Banks (2000) developed a flow model through synchronized flow visualization and pressure measurement that gives an index to describe the intensity of a conical vortex and explains the mechanism by which a vortex transfers the local flow velocity to roof suction. Tryggeson (2010) constructed an analytical model of the conical flow derived from a solution to the non-linear vorticity transport equation, predicting the resulting flow. This flow is then used to calculate suction on the attached surface.

In summary, the studies of the cause-and-effect relationship between the incident wind, the conical vortices and the induced roof suction are concentrated on qualitative assessments. Although the initial research on flow models of conical vortices has been conducted, the results have not been used to predict wind loads on large-span roofs exposed to conical vortices. Therefore, the aim of this study is to explain the mechanism of suction induced by vortices and to predict the suction beneath vortex cores. To address these topics, flow visualization of conical vortices and separation bubble was conducted in a wind tunnel using Particle Image Velocimetry (PIV). With the velocities in the vortices measured using PIV, the two-dimensional simplified flow model developed by Banks (2000) was improved and validated in this study. The intensities of the

separation bubble and conical vortices on a large-span roof were given for different wind directions. The quasi-steady theory was corrected by adding the effect of vortices. Finally, the mean and peak suction beneath the conical vortices and separation bubble was predicted by this improved flow model and validated by wind tunnel pressure measurements on a large-span flat roof.

2. Flow visualization of the separation bubble and conical vortices on a large-span flat roof

The PIV experiment was conducted to verify the existence of separation bubble and conical vortices on a large-span flat roof and to obtain the velocities in the vortices that would provide a basis for the establishment of the simplified flow model. This experiment was carried out in the HD-2 atmospheric boundary layer wind tunnel at the Wind Engineering Research Center of Hunan University, Changsha, China, where the working section is 17 m long, 3 m wide and 2.5 m high. The PIV system was provided by the Department of Mechanical and Vehicle Engineering at Hunan University.

Fig. 1 PIV experimental model of flat roof

Fig. 2 Steel bracket

2.1 Experimental model

Given the size of the laser section (800 mm×600 mm) in the PIV experiment, the model has a dimension of 450 mm×450 mm×180 mm (L×W×H), as shown in Fig. 1. To obtain a rigid body and avoid experimental error due to light reflection, the model was manufactured using black Plexiglas. Unlike in common pressure measurements, the model in a PIV experiment cannot be placed directly on the floor because of the 300 mm opaque side wall of the wind tunnel, which obstructs the view of the CCD camera. Therefore, a steel bracket (shown in Fig. 2) with a height of 510 mm was designed to elevate the model above the opaque side wall by setting it on the bracket, ensuring that the intense laser illuminates the model.

2.2 Experimental facilities

The PIV system used for this study is composed of software and hardware devices. The software system, Micro Vec V3.2.1, is compatible with Tecplot (graphics software) and Origin (mathematical analysis software). It includes an integrated particle image velocimetry system, an analysis system for measuring concentration field and particle diameter, and a control system for a digital camera. The hardware system is comprised of a Nd-YGA Laser system, a high resolution CCD camera, a synchronizer, an image acquisition card, and a personal computer.

The Nd-YGA Laser system was set above the roof of the HD-2 wind tunnel. The laser illuminated the flow field through the transparent glass roof, which resulted in light sheets parallel to the incident flow. The CCD camera was located outside the wind tunnel and normal to the flow direction. To ensure the integrity of the vortex profiles, the camera was set at a height of 780 mm from the ground, which was 90 mm higher than the flat roof located on the bracket.

Before the PIV experiment began, the suburban terrain (Category B) formulated in the *China loading code for the design of building structures* (*GB50009-2001*) was simulated by placing roughness elements in the entrance portion of the test section. At the roof height of 690 mm, the mean velocity and the longitudinal turbulence intensity were 10 m/s and 15%, respectively. After completing the simulation of the terrain, seeding particles with diameters of less than 1 μm were released into the wind tunnel from the exit.

The CCD camera initiated when the seeding particles in the wind tunnel were widely distributed. Two pairs of images were captured per second, and for each case, 100 images (50 velocity fields) were captured and processed. The post processing of the images was carried out by Micro Vec V3.2.1. The size of the interrogation window was selected as 64×64 pixels. After that, ensemble averaging of these 50 data files was conducted and imported to Tecplot Program. The streamlines and vorticity fields provided in Section 2.4 of this study were obtained after ensemble averaging.

2.3 Experimental design

The design of this PIV experiment is illustrated in Fig. 3, which considers the configuration of the separation bubble and conical vortices. For the separation bubble, the light sheet was located at the longitudinal bisector of the roof, shown in Fig. 3(a). This location was selected to avoid disturbance due to body-induced turbulence (Kasperski *et al*. 1996) near the edge of the roof. For the conical vortices, the light sheet was set at one side of the roof diagonal, parallel to the flow (Fig. 3(b)).

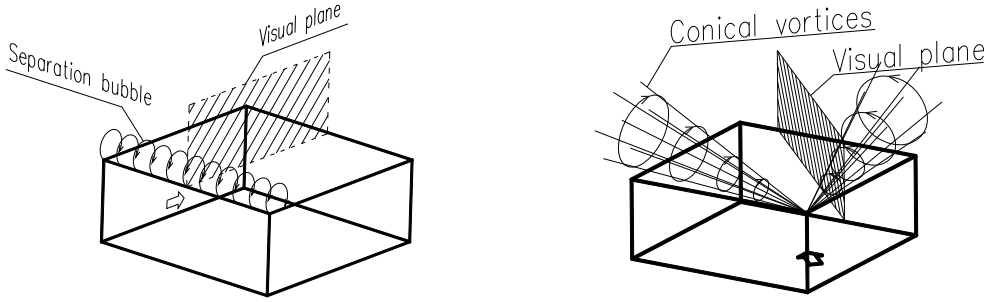

(a) Separation bubble (b) conical vortices

Fig. 3 Design of PIV experiment

2.4 Results and discussion

2.4.1 Separation bubble

The separation bubble is generated when the flow is normal to the leading edge (Zhao 1997) (wind direction of 0°). The position of the model in the wind tunnel is shown in Fig. 4 and the location of the light sheet is illustrated in Fig. 4(a).

The streamlines in the visual plane of the separation bubble are given in Fig. 5(a), which shows that the flow separates at the leading edge and reattaches to the roof surface to generate a separation bubble. Also, irregular streamlines on top of the plane imply the existence of small-scale coherent structures in the turbulent flow. Fig. 5(b) shows both the streamlines and the vorticity field in the visual plane of the separation bubble. Positive vorticity exists on top of the plane. While the negative vorticities were distributed around the separation bubble, which is a favorable configuration for the generation of vortices, the peak negative vorticity corresponds to the vortex core of the separation bubble. The magnitude of the negative vorticity decreases downstream, indicating an attenuation of the separation bubble.

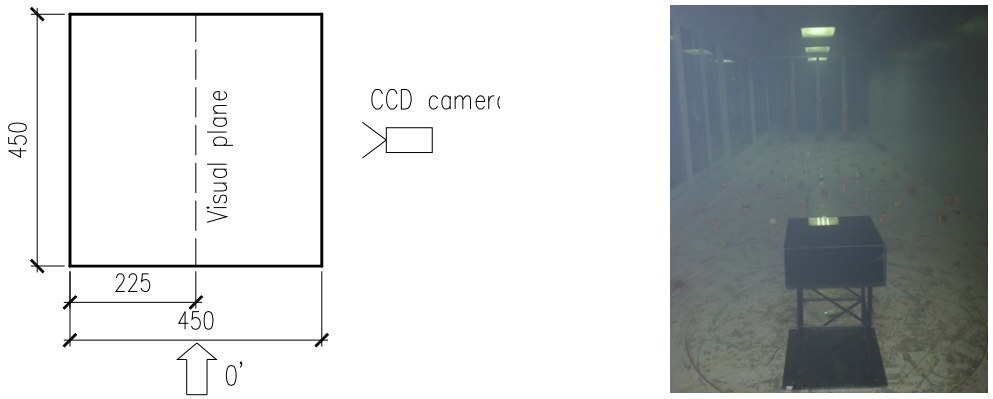

(a) Plan view (unit: mm) (b) physical position

Fig. 4 PIV experimental scheme for the separation bubble (wind direction of 0°)

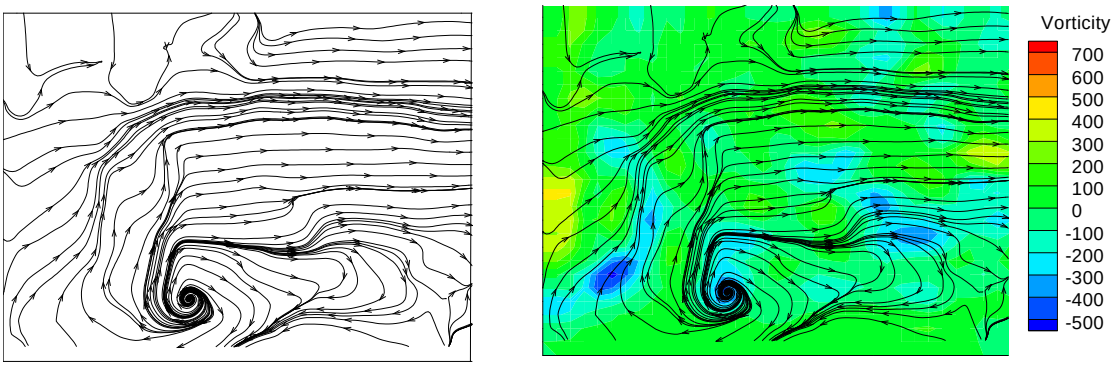

(a) Streamlines (b) vorticity field

Fig. 5 Streamlines and mean vorticity field of the separation bubble (wind direction of 0°)

2.4.2 Conical vortices

Conical vortices are generated along the leading edges of roofs when the flow attacks at oblique angles to the edge (Kawai and Nishimura 1996). Therefore, in this experiment, the wind directions used to observe conical vortices were set at 30° and 45°. The model was rotated to simulate different wind directions.

The arrangement of the model at a wind direction of 30° is shown in Fig. 6. It is known that conical vortices occur in pairs located on two sides of the diagonal of the roof. Research indicates that the size of a vortex close to the flow is larger than that at a greater distance from the flow (Zhao 1997 and Kim *et al*. 2001). Therefore, the visual plane was set on the right side of the diagonal (Fig. 6(a)).

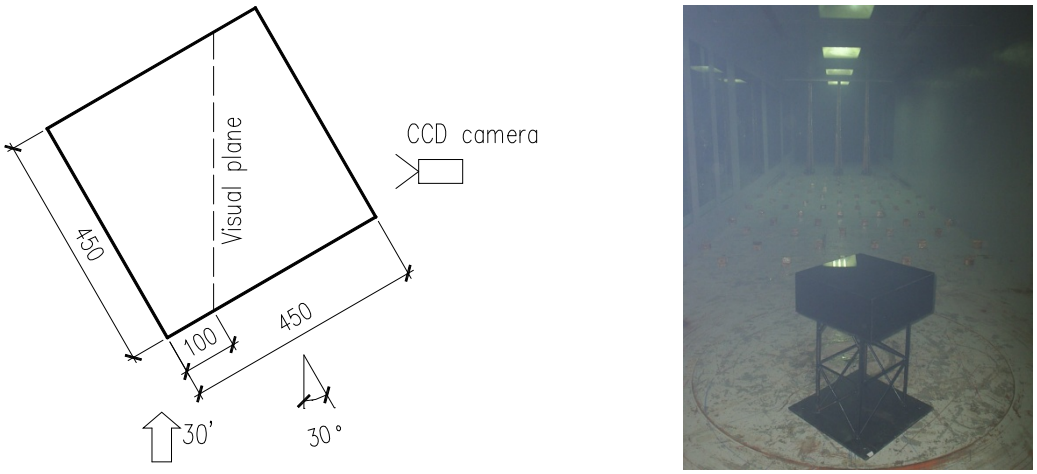

(a) Plan view (unit: mm) (b) physical position

Fig. 6 PIV experimental scheme for the conical vortex (wind direction of 30°)

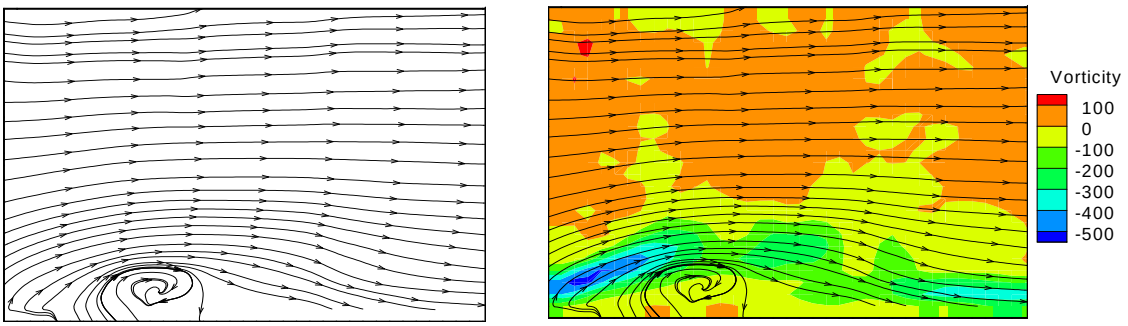

(a) Streamlines (b) vorticity field

Fig. 7 Streamlines and mean vorticity field of the conical vortex (wind direction of 30°)

The streamlines in the visual plane of the conical vortex at a wind direction of 30° are given in Fig. 7(a), which illustrates a conical vortex adhering to the roof. Fig. 7(b) shows both the streamlines and the vorticity field in the visual plane of the conical vortex. The negative vorticity was distributed over the roof, with its peak near the conical vortex. Greater suction is induced under this peak negative vorticity on the roof. The magnitude of the negative vorticity slightly decreased as it heads downstream. Positive vorticity is distributed uniformly on top of the plane, indicating no obvious effect from the vortices.

Fig. 8 shows the arrangement of the model at a wind direction of 45°. The flow was parallel to the diagonal of the roof. In symmetric structures, the conical vortices at the two leading edges of the roof have a very symmetric nature when the flow is running along the diagonal of the roof (Kawai 1997, Kim *et al*. 2001). In this experiment, the visual plane was set on the right side of the diagonal, as shown in Fig. 8(a).

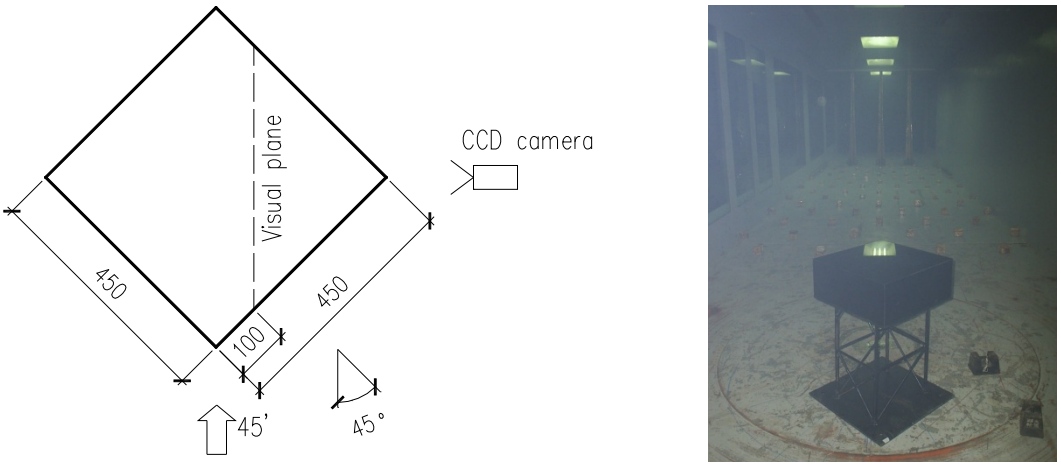

(a) Plan view (unit: mm) (b) physical position

Fig. 8 PIV experimental scheme for the conical vortex (wind direction of 45°)

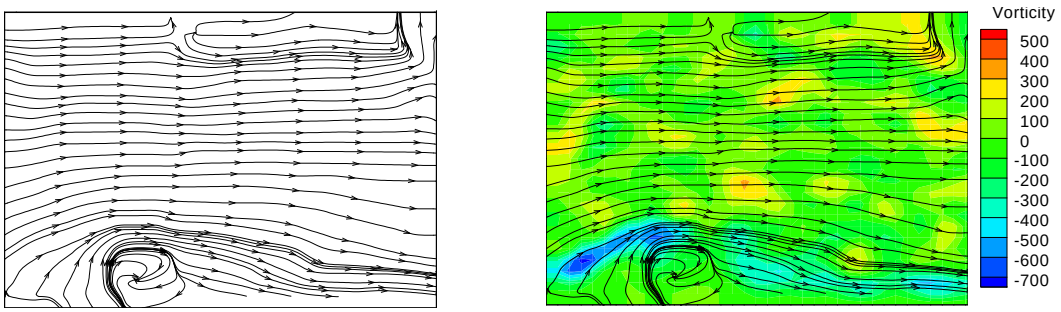

(a) Streamlines (b) vorticity field

Fig. 9 Streamlines and mean vorticity field of the conical vortex (wind direction of 45°)

The streamlines in the visual plane of the conical vortex at a wind direction of 45° are shown in Fig. 9(a). Compared with the oblong vortex at a wind direction of 30° (Fig. 7(a)), the conical vortex formed at a wind direction of 45° was more circular. Fig. 9(b) shows both the streamlines and the vorticity field in the visual plane of the conical vortex. The peak negative vorticity was located near the leading edge of the roof, which is favorable for the generation of a conical vortex. The negative vorticity and the intensity of the vortex attenuated slightly downstream.

3. Development of a flow model for conical vortices

3.1 Weaknesses of the existing vortex models

The existing vortex models used to predict pressure profiles are the point vortex, the Rankine vortex and Cook's simplified equation based on the Rankine vortex (Banks *et al*. 2000). In the point vortex model, the flow field is induced in potential flow theory by the placement of two counter-rotating vortices at a distance 2*h* from each other. The resulting surface flow velocity is given by

$$U(\xi) = \frac{\Gamma h}{\xi^2 + h^2} \tag{1}$$

Where Γ is circulation or strength of each vortex, *h* is the height of the vortex core and ξ is the projection distance along the roof surface (Fig. 10).

The point vortex model does describe the field-potential flow, but it is not realistic. The tangential velocity is predicted to increase infinitely as the vortex core is approached, which is misleading. Under the effect of the point vortex, surface pressures are assumed to simply follow the Bernoulli equation, which may lead to the underestimation of the actual pressures beneath vortices.

The Rankine vortex model (Fig. 11) is much more realistic than the point vortex model. It features a fully viscous vortex core rotating as a solid body and surrounded by an irrotational, inviscid vortex. The tangential velocities inside and outside the vortex core can be expressed as

$$U_{inner}(r) = cr / R^2 \tag{2}$$

$$U_{outer} = c / r \tag{3}$$

where c is a constant, R is the radius of the core (Fig. 11) and r is the distance from the center of the core (Fig. 11).

Therefore, the spin velocity in the vortex core increases with the increasing distance between the fluid particle and the center of the core, with the maximum velocity occurring at the boundary of the core. The velocity then decreases as a hyperbolic shape beyond the core. Fig. 11 gives the velocity profile of the Rankine vortex according to Eqs. (2) and (3). It is seen that the velocity changes abruptly at the boundary of the core, which is unrealistic. In fact, the vorticity of the circulating flow linearly increases in the core and then gradually decreases to zero outside the core (Simiu *et al*. 1996). This conclusion will be verified by the PIV experiment in the following section. Besides, the Rankine vortex does not adequately describe the flow field.

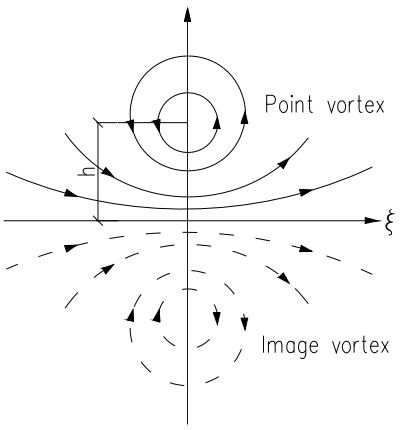

Fig. 10 Point vortex model

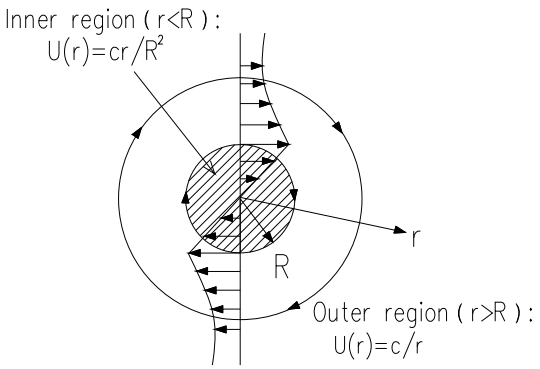

Fig. 11 Velocity profile of the Rankine vortex model

The Rankine vortex infers surface profiles for regions inside and outside the core (Banks *et al*. 2001). Cook (1985) approximates these two relationships with a uniform equation (Eq. (4)). However, the flow field is still unknown.

$$\frac{C_p}{C_{p\min}} = \frac{1}{1+\left(\frac{\xi}{R}\right)^2} \tag{4}$$

where C_p is the pressure coefficient for an arbitrary point on the pressure profile and $C_{p\min}$ is the minimum pressure coefficient (maximum suction coefficient) beneath the vortex core. The definitions of other symbols are given in Eqs. (1) and (2).

These models provide surface pressure profiles under vortices, but they offer little insight into the manner by which the turbulent component in the flow changes into roof suction. They also pay little attention to the flow field around the vortices. However, Banks (2001) developed a flow model of conical vortices that describes the relationship between the flow velocity above the vortex, the vortex and the roof surface. In this study, the flow model developed by Banks (2001) was improved and validated by simplifying the velocity profile between the vortex and the potential region. Based on this improved model, the intensities of the conical vortices and separation bubble on a large-span roof were quantified. Finally, the predictions for suction beneath vortex cores were given and verified.

3.2 Conception of the flow model for conical vortices

In potential flow theory, the flow field around a point vortex is induced by the placement of two counter-rotating vortices. Unlike this theory, the flow model in this study is imagined to be a wheel that is spun by the free stream above it (Banks *et al*. 2001). This flow model is similar to the Rankine vortex, but the velocity through the Rankine vortex changes abruptly and unrealistically at the boundary of the core (Xu 1985). Therefore, a transition region was added between the vortex region and the potential flow region, which maked the vorticity change gradually from increasing inside the vortex to decreasing outside the vortex. The schematic of this flow model is shown in Figs. 12(a) and 12(b) shows its velocity profile. The origin of the coordinates is set at O. Letting $a = \zeta / h$ (Fig. 12(a): ζ is the vertical distance from O and h is the height of the vortex core), this flow model can be divided into four regions(Banks *et al*. 2001): the viscous vortex core ($-0.2<a<0.2$), the vortex region ($0.2<a<1$ and $-1<a<-0.2$), the transition region ($1<a<2$) and the potential flow region ($a>2$).

According to aerodynamic theory, the pressure gradient through the vortex can be expressed as (Xu 1987)

$$\frac{dP}{dn} = \frac{\rho U^2}{R_c} \tag{5}$$

where dP/dn is the pressure gradient from point T to point B (Fig. 12(a)), U is the fluid speed in the direction of vortex rotation, R_c is the curvature radius of the streamlines in the vortex, and ρ is the air density.

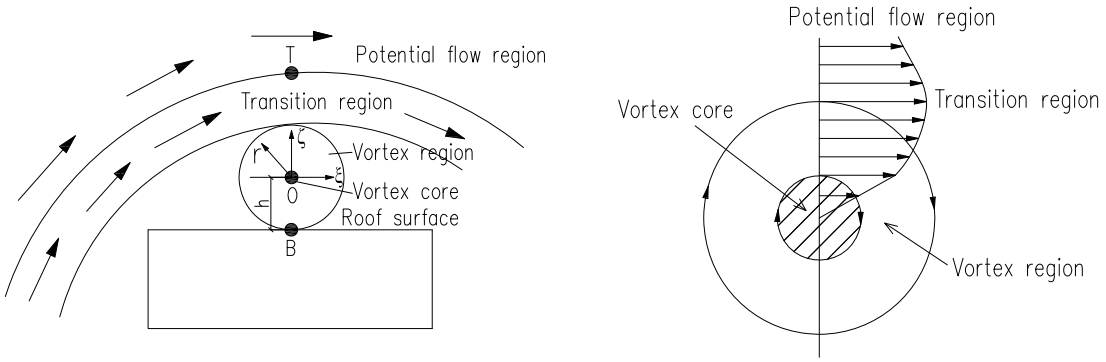

(a) Schematic (b) Velocity profile

Fig. 12 Two-dimensional flow model of the conical vortices

Hence, the pressure change through the vortex is associated with centrifugal accelerations. There is a quantitative relationship between the pressure change, the curvature radius of the streamlines and the rotational speed of the vortex. Eq. (5) provides a basic foundation for developing the flow model for conical vortices in this study, and the curvature radius of the streamlines and the velocity profile in the vortices are investigated below.

3.3 Curvature radius of the streamlines in a vortex

The curvature radius of the streamlines corresponding to different regions is described below.

- In the core, the fluid rotates as a solid body. $R_c = \zeta$, and the curvature radius of streamlines is

$$R_c / h = a \tag{6}$$

- As the flow beneath the vortex approaches the roof, the curvature radius becomes infinite. That is, $a \rightarrow$-1 and $R_c \rightarrow \infty$. Thus, the curvature radius of the streamlines between the core and the roof (-1<a<-0.2) can be expressed as

$$R_c / h = a / (1 + a) \tag{7}$$

- Above the vortex core, the flow will also tend to be straight line and eventually merge with the incident flow around the roof. Through CFD numerical simulation, Banks (2000) gave the curvature radius of the streamlines for regions above the core (a>0.2) as

$$R_c / h = a + \frac{1}{2} a^3 \tag{8}$$

3.4 Velocity profile in a vortex

The velocity profile through the vortex is described in the following steps.

- In the vortex core, viscosity dominates and the flow rotates as a solid body. The velocity

U increases linearly with r

$$U = \omega \cdot r \tag{9}$$

where ω is a proportionality constant.

- The velocity profile in the vortex region is based on Rizzi's numerical solution of the complete N-S equations for a 65° sweep delta-wing at an attack angle of 10° (Rizzi and Muller 1989). The equation is

$$\frac{U}{U_T} = a^{1/2} \tag{10}$$

Substituting Eq. (10) into Eq. (5), the pressure is seen to vary linearly with a. This linear variation agrees well with numerical simulation results (Ekaterinaris and Schiff 1994). It should be noted that the suction decreases from the core toward the roof surface. According to Eq. (5), this decrease is slow beneath the core because the curvature radius of the streamlines increases rapidly as it nears the roof surface. Therefore, most suction in the vortex core will be transferred to the roof surface.

- In the potential flow region, the Bernoulli equation should be obeyed. Banks provides the following equation(Banks 2001)

$$\frac{U}{U_T} = \sqrt{e^{\left(\int_{a_T}^{a} \frac{-2}{(R_c/h)} dn\right)}} \tag{11}$$

- In the transition region, the maximum velocity is at $a_{\max} = 1.5$ (Banks *et al*. 2000). To achieve a smooth transition and ensure the location of the peak velocity, Banks proposed the following velocity equation

$$U = \frac{U_{\max} \cdot 2 \cdot \left(a / a_{\max}\right)}{1 + \left(a / a_{\max}\right)^2} \tag{12}$$

where $U_{\max} = 1.05 U_T$.

The measured velocities in the vortices during the PIV experiment were fitted based on the above equations. To match those velocities at the boundary points of different regions, constant terms may be added to the fitting equations and the slope of curves was adjusted slightly. Eqs. (9) and (10) were adopted for the fitting of velocities in the vortex core (-0.2<a<0.2) and the vortex region (-1<a<-0.2 and 0.2<a<1), respectively. Eq. (11) was employed in the potential flow region. Considering that Eq. (12) was complex, the parabolic equation (Eq. (13)) was used for the fitting of velocities in the transition region (1<a<2).

$$U / U_T = Aa^2 + Ba + c \tag{13}$$

The above velocity profiles were used to fit the measured velocities in vortices during the PIV experiment, as shown in Fig. 13. For comparison, the velocity profile of the Rankine vortex was also given in Fig. 13. It should be noted that the measured velocities were an ensemble average of the instantaneous data under wind directions of 0°, 30° and 45°. The results indicated that the velocities in the transition region can be satisfactorily fitted by the parabolic equation, which leads to a smooth transition in the velocity profile.

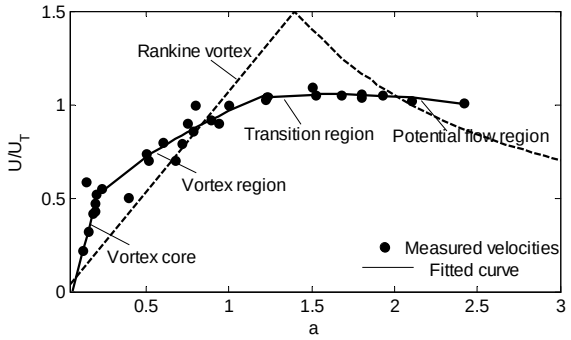

Fig. 13 Fitting of velocities in the vortices

Table 1 Curvature radius of streamlines and velocity profiles in the vortices

Region	Range	R_c/h	U/U_T	
			Flow model of this study	Banks model
Vortex region beneath the core	$-1 < a < -0.2$	$a/(a+1)$	$-(0.1403+0.8199\sqrt{-a})$	$-0.9\sqrt{-a}$
Vortex core	$-0.2 < a < 0.2$	a	$3.4292 \cdot a$	$2.15a$
Vortex region above the core	$0.2 < a < 1$	$a+a^3/2$	$0.1403+0.8199\sqrt{a}$	$0.9\sqrt{a}$
Transition region	$1 < a < 2$	$a+a^3/2$	$-0.1254a^2+0.4374a+0.6737$	$\frac{3.15a}{2.25+a^2}$
Potential flow region	$a > 2$	$a+a^3/2$	$\sqrt{\exp(\int_{a_3}^{a}\frac{-2}{(R_c/h)}da)}$	$\sqrt{\exp(\int_{a_3}^{a}\frac{-2}{(R_c/h)}da)}$

Note: R_c -Curvature radius of streamlines; h -Height of vortex core; U -Rotation velocity of vortex; U_T -Velocity at T of potential flow region

Table 1 shows the curvature radius of the streamlines R_c/h (Section 3.3) and the fitted equations for the velocities U/U_T. For comparison, the equations for U/U_T provided by Banks (2000) are also shown in Table 1. In Section 4 of this study, Banks' model was compared with the improved model to predict mean and peak suction beneath the conical vortices and separation bubble.

The goodness of fit statistics for Fig. 13 are given in Table 2 and described below. (1) SSE is the sum of squares due to error. A value closer to 0 indicates a better fit. (2) The R-square measures how successful the fit is in explaining the variation of the data. It is the ratio of the sum of squares of regression (SSR) and the total sum of squares (SST). A value closer to 1 indicates a better fit. (3) The adjusted R-square uses the R-square statistic defined above and adjusts it based on the residual degrees of freedom. A value closer to 1 indicates a better fit. (4) The RMSE is the root mean squared error. A value closer to 0 indicates a better fit.

Table 2 Goodness of fit statistics

Region	Range	SSE	R^2	Adjusted R^2	RMSE
Vortex core	$0 < a < 0.2$	0.0015	0.9684	0.9526	0.0275
Vortex region above the core	$0.2 < a < 1$	0.0088	0.9419	0.9347	0.0332
Transition region	$1 < a < 2$	0.0004	0.9823	0.9704	0.0038
Potential flow region	$a > 2$	0.0002	0.9766	0.9668	0.0027

3.5 Pressure change in a vortex

Through the integration of Eq. (5), the pressure change from point T towards point B (Fig. 12 (a)) along the ζ axis can be expressed as (Banks *et al*. 2000)

$$\int_T^B dP = \int_T^B \frac{\rho U^2}{\left(R_c / h\right)} da \tag{14}$$

Normalizing by the reference dynamic pressure and U_T gives

$$Cp_B = Cp_T - \frac{U_T^2}{U_{ref}^2}\left[2\int_B^T \frac{U^2(a)}{U_T^2\left(R_c(a)/h\right)} da\right] \tag{15}$$

Point T is located in the potential flow region; therefore, Cp_T can be calculated using the Bernoulli equation, $P_T - P_{ref} = 1/2\rho\left(U_{ref}^2 - U_T^2\right)$. The basic definition of pressure coefficient is also used, so

$$Cp_T = \frac{P_T - P_{ref}}{\frac{1}{2}\rho U_{ref}^2} = 1 - \frac{U_T^2}{U_{ref}^2} \tag{16}$$

Substituting Eq. (16) into Eq. (15) gives

$$Cp_B = 1 - \frac{U_T^2}{U_{ref}^2}\left[1 + 2\int_B^T \left(\frac{U}{U_T}\right)^2 \left(\frac{R_c}{h}\right)^{-1} da\right] \tag{17}$$

Let $\Delta Cp = 1 - Cp$. According to Eq. (16), $\Delta Cp_T = \left(U_T / U_{ref}\right)^2$. Thus, ΔCp_B is given as

$$\Delta Cp_B = \Delta Cp_T\left[1 + 2\int_B^T \left(\frac{U}{U_T}\right)^2 \left(\frac{R_c}{h}\right)^{-1} da\right] \tag{18}$$

It can be seen that there is a transfer function between the pressures at point T and point B, which implies an amplification factor related to the pressure change from the potential flow region

to the roof surface.

To investigate the amplification factor, letting

$$\eta = 2\int_B^T \left(\frac{U}{U_T}\right)^2 \left(\frac{R_c}{h}\right)^{-1} da \tag{19}$$

Eq. (18) can then be written as

$$\Delta Cp_B = (1+\eta)\Delta Cp_T \tag{20}$$

Eq. (20) implies that the vortex amplifies and transfers pressures above the vortex to the roof surface. The amplification factor η demonstrates the intensity of the vortices. A larger η corresponds to an intense vortex and greater roof suction. If $\eta = 0$, there is no obvious vortex on the roof. From Eq. (19), it can be seen that a larger curvature radius of streamlines causes greater suction beneath vortices. The faster the vortex spins, the greater the roof suction becomes. Therefore, vortices control roof suction through the curvature radius of streamlines and rotational velocity.

Because η is related to the curvature radius of streamlines R_c, η represents not only the vortex strength but also the nature of the reattachment. A larger curvature of streamlines means stronger vortices and obvious reattachment.

3.6 Corrections based on wind direction

Experimental measurements show that the wind changes direction as it passes over the leading edge of a roof. Fig. 14 illustrates the actual wind direction imposed on the conical vortex. It is indicated that the tangential speed above the vortex should be $U \cdot \sin(\alpha)$. α is the actual wind angle with respect to the vortex axis and ω is the experimental wind angle.

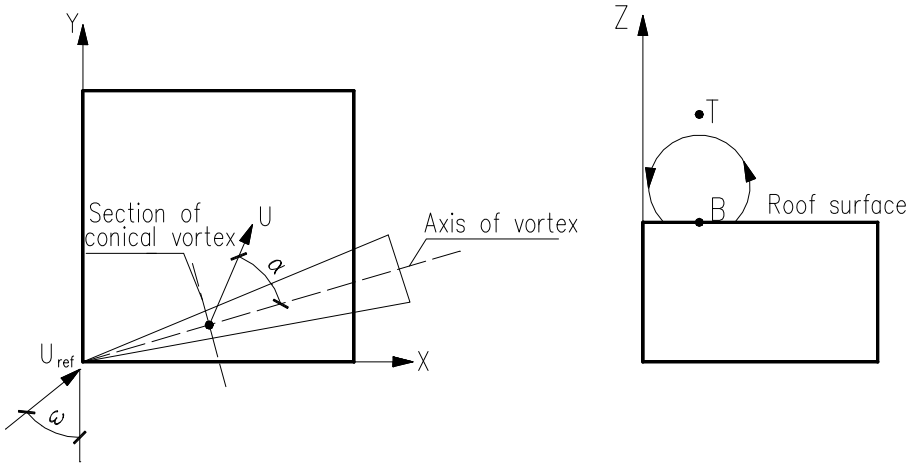

(a) Top view (b) side view

Fig. 14 Variation of tangential speed

The flow model was corrected by considering the actual wind angle. U in Eq. (17) is substituted with $U \cdot \sin(\alpha)$. Combining Eqs. (17) and (19) gives (Banks *et al*. 2000)

$$Cp_B = 1 - \frac{U_T^2}{U_{ref}^2}\left[1 + \sin^2(\alpha) \cdot \eta\right] \tag{21}$$

Through flow visualization, Banks gave the relationship between α and ω

$$\alpha = 18 + 0.7\omega \tag{22}$$

Based on Eq. (21), the mean pressure at point B (beneath the vortex core) can be written as

$$\overline{Cp_B} = 1 - \frac{\overline{U_T^2}}{\overline{U_{ref}^2}}\left(1 + \sin^2(\alpha) \cdot \eta\right) \tag{23}$$

The quasi-steady theory is a simple, practical model used to describe the relationship between the incident flow and roof pressure. It is the basis for wind-resistant codes in many countries, and links the pressure fluctuations on roofs directly to fluctuations in the approaching flow

$$C_P(t) = \left(\frac{U_{ref}(t)}{\overline{U_{ref}}}\right)^2 \overline{C_p}\left(\omega(t)\right) \tag{24}$$

where $U_{ref}(t)$ is the time history of the wind velocity at the reference point, $\overline{U_{ref}}$ is the mean velocity at the reference point, $\omega(t)$ represents the wind direction of the incident flow and $\overline{C_p}\left(\omega(t)\right)$ is the mean pressure at a certain point of study.

However, many studies have concluded that the quasi-steady theory fails to accurately predict pressures in separation regions, such as beneath conical vortices (Banks *et al*. 2000). This is because the quasi-steady theory attributes the roof pressure fluctuations to the fluctuating content of the incident flow and ignores the effect of conical vortices (as shown in Eq. (24)). Therefore, fluctuating and peak pressures are underestimated by the quasi-steady theory. To correct the quasi-steady theory, the effect of conical vortices is added; that is, Eq. (23) is substituted into Eq. (24)

$$Cp_B(t) = \left(\frac{U_{ref}(t)}{\overline{U_{ref}}}\right)^2 \left(1 - \frac{\overline{U_T^2}}{\overline{U_{ref}^2}}\left[1 + \sin^2(\alpha) \cdot \eta\right]\right) \tag{25}$$

Therefore, the incident flow, the vortices and the roof pressures are connected by Eq. (25). If $U_{ref}(t)/\overline{U_{ref}}$, on the right side of the equation, is taken as the ratio of the peak velocity to mean velocity $U_{ref\,\max}(t)/\overline{U_{ref}}$, the Cp_B obtained on the left side of the equation is the peak suction beneath the vortex cores. Eqs. (23) and (25) were used to predict mean and peak suction beneath cores of the conical vortices and separation bubble to verify the effectiveness of this flow model.

4. Verification of the flow model

4.1 Wind tunnel pressure measurement on a large-span flat roof

Pressure measurement on a large-span flat roof was performed in the TJ-2 atmospheric boundary layer wind tunnel at the State Key Laboratory for Disaster Reduction in Civil Engineering of Tongji University, Shanghai, China, with the goal of validating the improved flow model described in the previous section. The working section is 17 m long, 3 m wide and 2.5 m high. The flat roof (Fig. 15(a)) has a platform measuring 750 mm×750 mm×300 mm that was manufactured using Plexiglas to obtain a "rigid" body. It was a larger-scale model of the flat roof used in the PIV experiment (Fig. 1). Fig. 15(b) illustrates the tap locations and the angles of incidence. The suburban terrain (Category B) formulated by *GB50009-2001* was simulated, and the velocity of the approaching flow was measured simultaneously with the pressure. At a reference height of 300 mm, the mean wind velocity and the longitudinal turbulence intensity were 10 m/s and 15%, respectively.

The measured pressures were converted to pressure coefficients by dividing them by the reference dynamic pressure at the reference height of 300 mm.

$$C_{pi}(t)=\frac{P_i(t)-P_\infty}{P_0-P_\infty} \tag{26}$$

where $P_i(t)$ is the measured pressure at tap i, P_0 is the total pressure at the reference height and P_∞ is the static pressure at infinity.

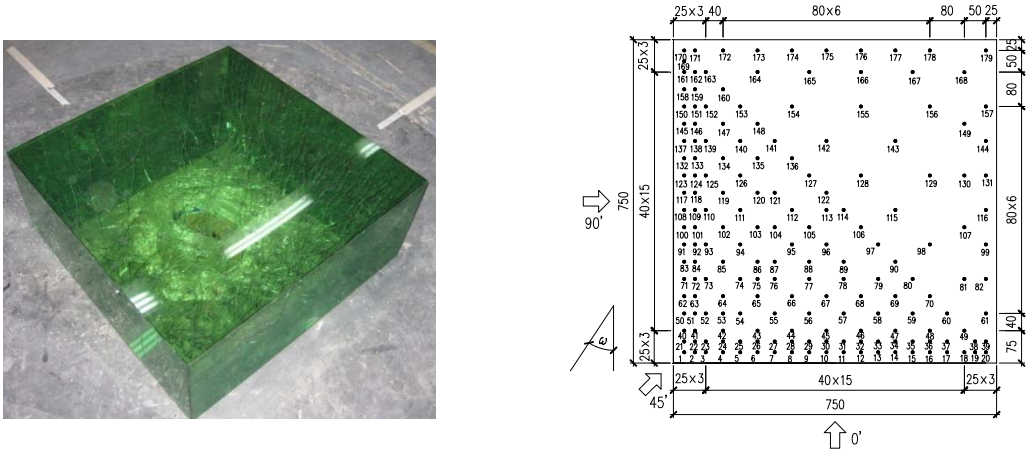

(a) Physical model (b) tap locations (unit: mm)

Fig. 15 Model of the flat roof and its tap locations

Table 3 Integration for intensity of the conical vortices (wind direction of 15°)

Flow model	Region	Integration results	Total intensity
Flow model in this study	-1<a<-0.2	0.69	2.8
	-0.2<a<0.2	0	
	0.2<a<1	1.396	
	1<a<2	0.72	
Banks' model	-1<a<-0.2	0.518	2.34
	-0.2<a<0.2	0	
	0.2<a<1	1.088	
	1<a<2	0.729	

By measuring the pressures on the flat roof, the wind directions that favor the generation of conical vortices can be determined. It has been demonstrated (Kawai and Nishimura 1996, Banks 2000) that the profiles of the mean pressure coefficient along lines normal to the eaves are bell-shaped under the influence of conical vortices. This conclusion is in agreement with the theory of the point vortex in fluid mechanics (Lin *et al*. 2005). Therefore, the question of whether pressure profiles along lines normal to the leading edge are bell-shaped is utilized to judge the formation of conical vortices in this study. If the profiles are approximately bell-shaped, the roof is identified as being under the influence of conical vortices; otherwise, there are no conical vortices on the roof. Then the mean pressure profiles for lines normal to the leading edge were analyzed at wind directions ranging from 0° to 90°. It is concluded that the angles conducive to the formation of conical vortices on the flat roof are 15°, 30°, 45°, 60° and 75°. Under wind directions of 0° and 90° (normal to the leading edge), separation bubble is generated instead(Zhao 1997).

4.2 Intensity of the conical vortices

The intensities of the conical vortices in different directions were integrated using Eq. (19), with an integration range of [-1,2]. Table 1 shows the rotational velocity and the curvature radius of the streamlines in the vortices. As an example, the intensity of the conical vortices at a wind direction of 15° was integrated and given in Table 3. For comparison, the integration of the vortex strength based on Banks' model (Banks *et al*. 2000) was also shown in Table 3. The integral function was given in Table 1.

It is clear that intensity of the vortex region above the core (0.2<a<1) constituted the largest percentage of the total strength. In the vortex region (-1<a<-0.2 and 0.2<a<1), the intensities calculated by the flow model of this study were higher than those calculated by Banks' model. In the transition region, the intensities provided by the two flow models were nearly the same.

After the integration of vortex strength at a wind direction of 15°, the intensities of conical vortices at wind directions of 30°, 45°, 60° and 75° were analyzed. According to Eq. (19), the rotational velocity and curvature radius of the streamlines are two factors that influence the vortex strength. As mentioned in Section 3.4, the equations for rotational velocity in vortices were obtained from numerical simulations (Rizzi *et al*. 1989, Ekaterinaris *et al*. 1994), which were assumed to be invariant. Thus, the vortex strength was only influenced by the curvature radius of the streamlines. In this study, the curvature radius of the streamlines was estimated by the angle between the vortex axis and the leading edge. Then the ratio of vortex strength between different

wind directions can be estimated by the ratio of the angle between the vortex axis and the leading edge. Several studies have indicated that the maximum mean suction in pressure profiles is directly beneath the vortex core (Kawai *et al*. 1996). The connection of the vortex cores can be assumed to approximate the axis of the conical vortex. The pressure profiles for lines normal to the leading edge were calculated using this knowledge. The vortex axis on the large-span flat roof under various wind directions was demonstrated in Fig. 16.

At wind directions of 30° and 15°, the ratio of the angle between the leading edge and the vortex axis was 7/8. As mentioned in Table 3, the vortex strength at a wind direction of 15° was 2.8. Thus, the vortex strength at a wind direction of 30° was $2.8\times(7/8)=2.45$. The intensities of the conical vortices under different wind directions were similarly estimated (Table 4) using the reference intensity of 2.8 (wind direction of 15°). Table 4 also gives the intensities of the conical vortices based on Banks' model (Banks *et al*. 2000).

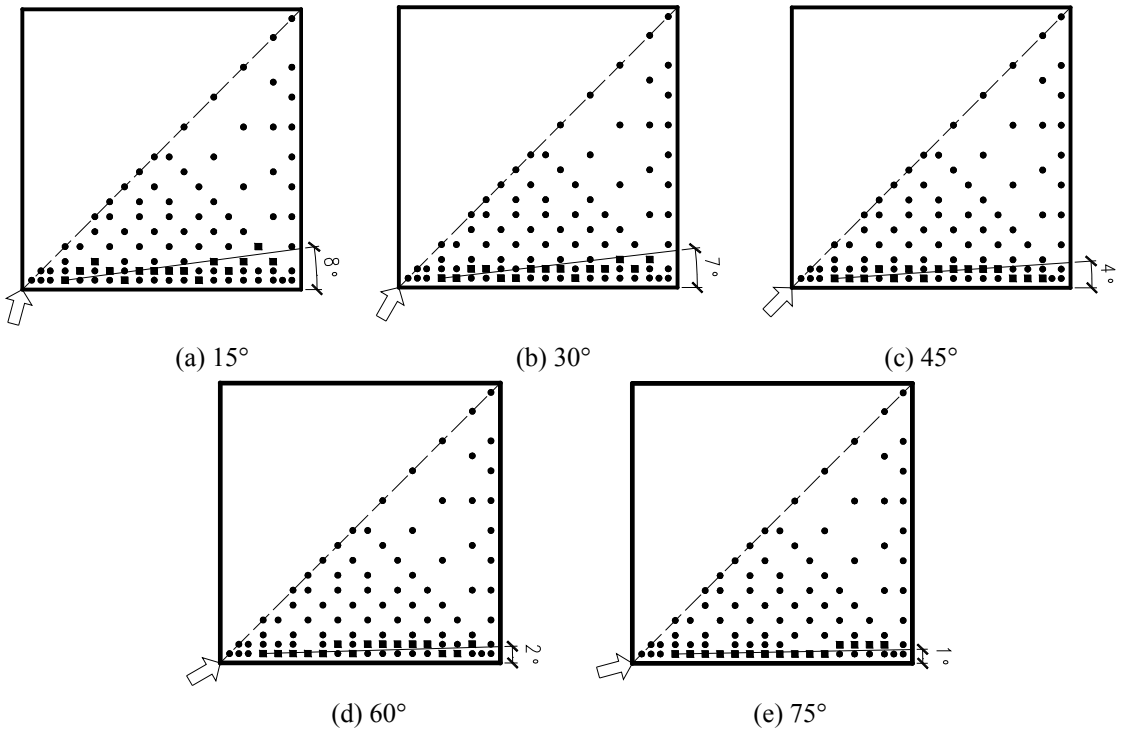

(a) 15° (b) 30° (c) 45°

(d) 60° (e) 75°

Fig. 16 Vortex axis of the conical vortices at different wind directions

Table 4 Intensities of the conical vortices at different wind directions

Wind direction	15°	30°	45°	60°	75°
Flow model in this study	2.8	2.45	1.4	0.7	0.35
Banks' model	2.34	2.05	1.17	0.585	0.29

Table 4 shows that the intensities calculated with the flow model of this study were larger than those obtained from Banks' model. Therefore, the resulting suction beneath the vortex cores was expected to be larger based on the improved flow model. By comparing these results with measured pressures on the large-span flat roof, the following discussion will evaluate the effectiveness of these two models in predicting suctions beneath vortex cores.

4.3 Variation of the rotational velocity in the longitudinal direction

The rotational velocity $\overline{U_T}/\overline{U_{ref}}$ above the vortices decreases with increasing distance from the windward corner. Banks determined the variation of $\overline{U_T}/\overline{U_{ref}}$ along the leading edge at a wind direction of 30°(Banks, 2000), which was fitted as shown in Fig. 17. Note that the attenuation is parabolic and can be expressed by Eq. (27)

$$\overline{U_T}/\overline{U_{ref}} = 7.17\times10^{-6}X^2 - 0.003X + 1.59 \tag{27}$$

where X is the distance between the apex and the section of the conical vortex (Fig. 18).

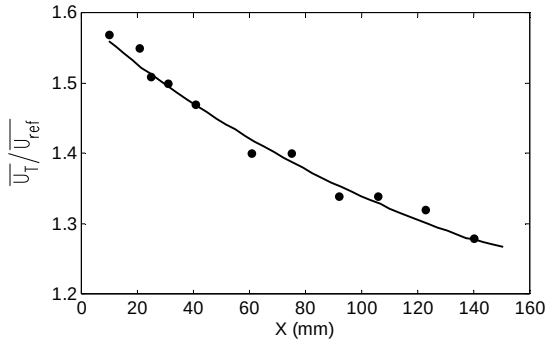

Fig. 17 Fitting of the velocity in the longitudinal direction

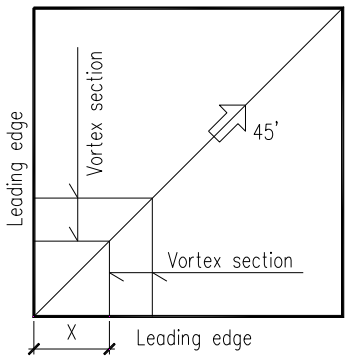

Fig. 18 Planar projection of the conical vortices

4.4 Prediction of mean suction beneath the cores of the conical vortices ($\overline{Cp_v}$)

The mean suctions beneath the cores of the conical vortices ($\overline{Cp_v}$) were calculated using Eq. (23), in which:

1) η was shown in Table 4.

2) $\overline{U_T}/\overline{U_{ref}}$ was calculated according to Eq. (27). However, Eq. (27) was proposed based on a wind direction of 30°. Through flow visualization, Banks gave the variation of $\overline{U_T}/\overline{U_{ref}}$ with wind direction (Banks *et al*. 2000), as shown in Fig. 19. Therefore, in this study, the values for $\overline{U_T}/\overline{U_{ref}}$ under other wind directions were discounted based on the curve in Fig. 19. It should be noted that the roof models in this study and in the literature (Banks *et al*. 2000) were different in size, so the X value in Eq. (27) has been prorated according to the size ratio of the two models.

Conditional sampling should be conducted in order to obtain the measured value for $\overline{Cp_v}$ because the vortex cores move back and forth and the maximum suction is found to follow the moving cores directly (Kawai and Nishimura 1996, Banks and Meroney 2001a, b, c). There were several taps on a section of the conical vortices in this experiment. At each instant, the tap having the maximum suction was selected, and this maximum suction was extracted to form a new time history called the pressure time series of the vortex core. The mean of this new time series can be set as the measured value of $\overline{Cp_v}$.

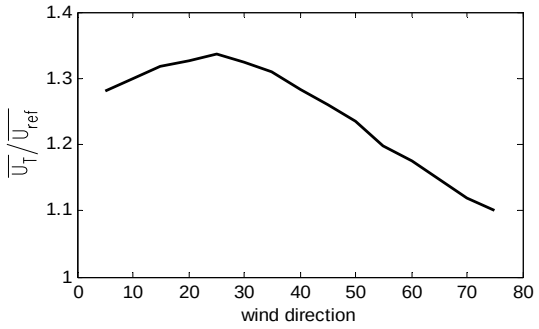

Fig. 19 Variation of velocity with wind direction

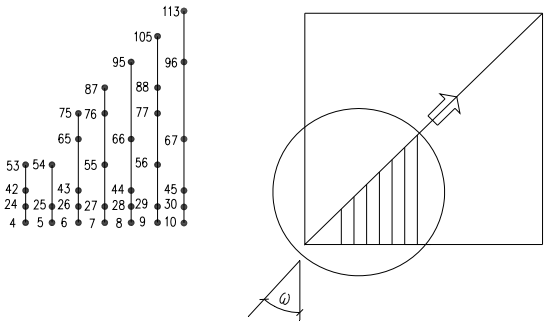

Fig. 20 Typical section of the conical vortices

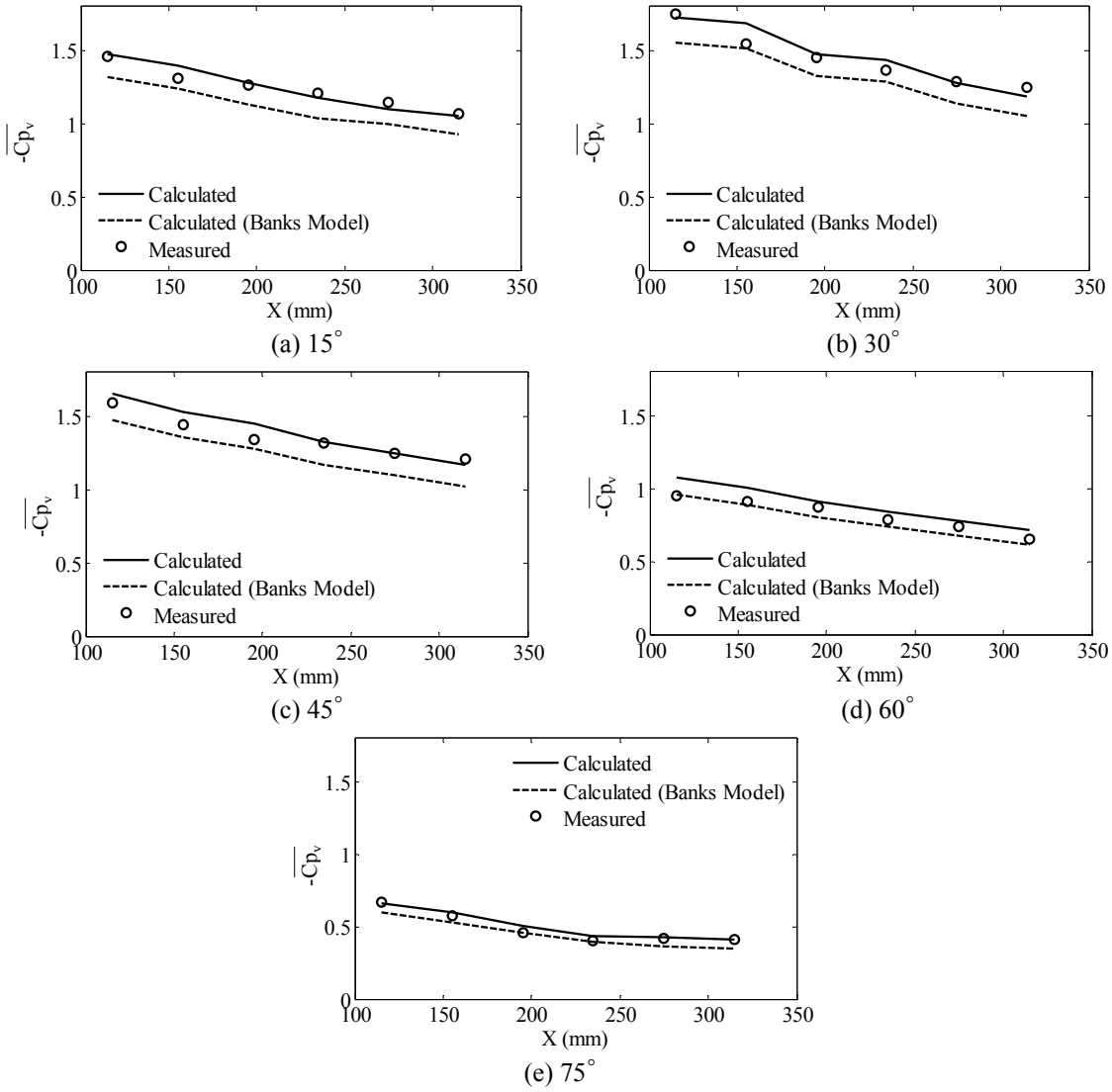

Fig. 21 Comparison of the calculated and measured mean suction beneath cores of the conical vortices

Several sections of conical vortices were randomly selected as research objects (Fig. 20, in which the section number is the number of the tap on the leading edge). At different wind directions, the mean suction beneath the cores of these sections (Col. 4-Col. 9) was calculated using Eq. (23) and compared with the measured values, as shown in Fig. 21. For comparison, the calculated results given by Banks' model were also shown in Fig. 21.

The following conclusions can be drawn from Fig. 21:

- The mean suction beneath the cores of the conical vortices is largest at a wind direction of 30° because the lateral component of the approaching turbulence increases when the flow deviates from the diagonal of the roof at a wind angle of 30° (Fig. 22). Fig. 19 also

demonstrates that $\overline{U_T}/\overline{U_{ref}}$ above the vortices reaches a maximum at a wind direction of nearly 25°. Therefore, the rotational speed is the dominant factor for suction beneath the vortex cores. This result also can be confirmed by the frequency domain. Fig. 23 shows the wind pressure spectra at tap 42 (randomly selected in the vortex area, Fig. 15(b)) for different wind directions. It can be seen that the highest peak occurs at a wind direction of 30°. In other words, the largest fluctuating energy in the approaching flow induces the greatest mean suction beneath the vortex cores.

- For conical vortices at the given direction, the suction beneath the conical vortices decreases as the distance from the apex increases, with the peak occurring near the windward corner. This is due to the fact that the curvature radius R_c decreases and the rotational speed $\overline{U_T}/\overline{U_{ref}}$ increases towards the apex. The mean suction is expected to increase, according to Eq. (23), so the smaller vortices would induce greater suction near the leading corner.
- Because of the larger vortex strength given by the flow model in this study (Table 4), the calculated mean suction was greater than that given by Banks' model. Compared with the measured values, the errors in the predictions based on the improved model were less than 10%. Some of the predicted suction was larger than the measured results. Errors for the calculated results given by Banks' model were generally less than 15%. Therefore, the mean suction given by the improved model is more accurate than that from Banks' model.

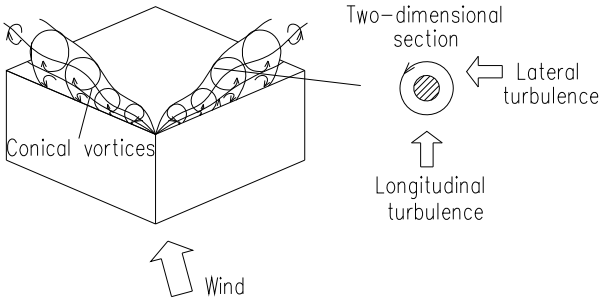

Fig. 22 Schematic of the incident flow on the conical vortices (wind direction of 30°)

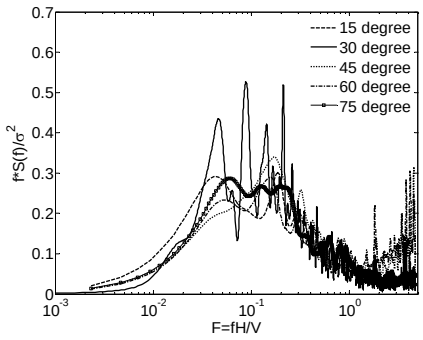

Fig. 23 Pressure spectra induced by different wind directions

4.5 Prediction of peak suction beneath the cores of the conical vortices ($Cp_{v\max}$)

The peak suction beneath the cores of the conical vortices was calculated using Eq. (25), which is the corrected quasi-steady theory. The calculation of the mean suction has been presented in Section 4.4. The ratios of the maximum to mean velocity of the incident wind ($U_{ref\max}(t)/\overline{U_{ref}}$) were obtained from the measured upstream velocities, as shown in Fig. 24, and the mean velocity was limited to 10 m/s. The ratios of $U_{ref\max}(t)/\overline{U_{ref}}$ under different wind directions are given in Table 5.

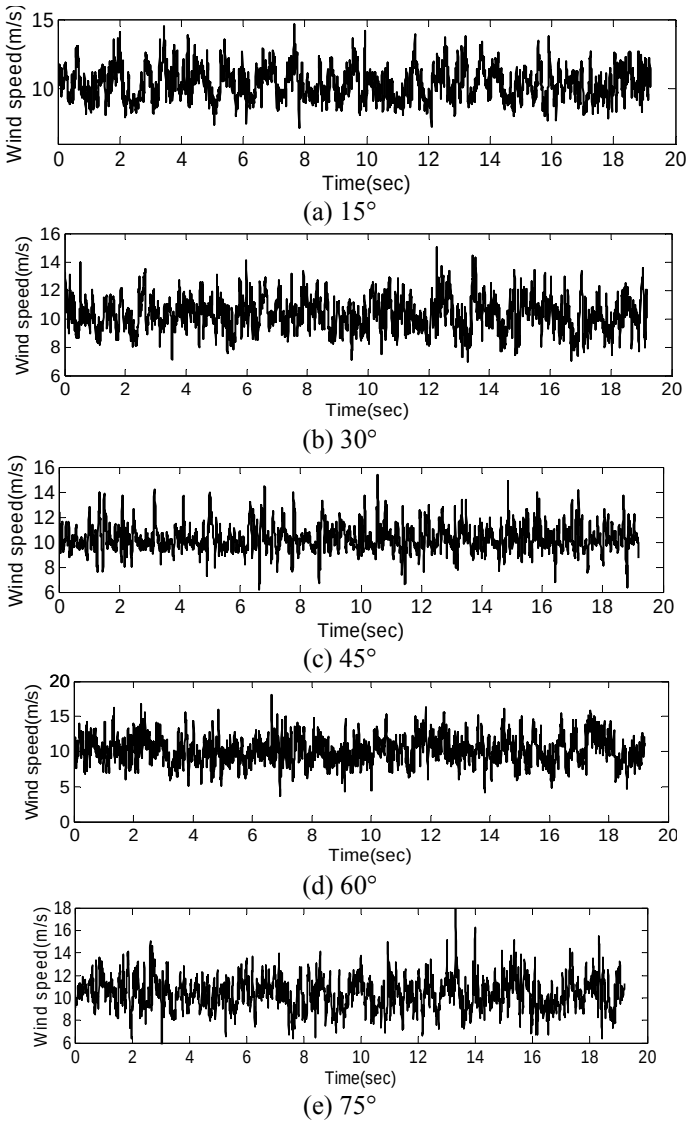

Fig. 24 Incident velocities at different wind directions

Table 5 Ratios of maximum to mean velocity at different wind directions

Wind direction	15°	30°	45°	60°	75°
$U_{ref\,\max}(t)/\overline{U_{ref}}$	1.47	1.51	1.50	1.78	1.79

The typical sections shown in Fig. 20 continue to be used as research objects. The peak suction beneath the cores of these sections (Fig. 20: Col. 4-Col. 9) were calculated using Eq. (25). The calculation results were compared with the measured values that select the maximum in the pressure time series after conditional sampling (as mentioned in Section 4.4). Fig. 25 demonstrates the results of comparing the calculated and measured peak suction beneath the cores of the conical vortices. For clarity, the calculated results given by Banks' model are also shown in Fig. 25.

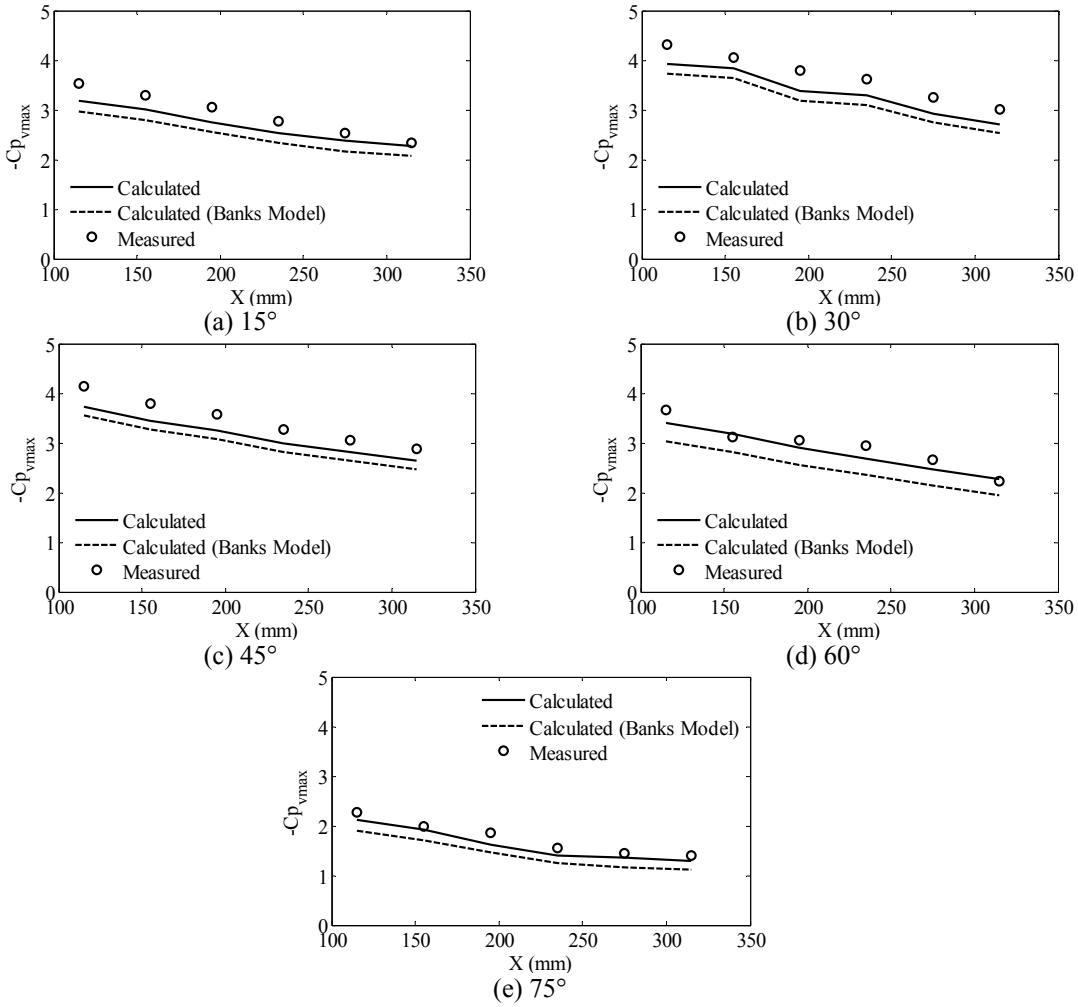

Fig. 25 Comparison of the calculated and measured peak suction beneath the cores of the conical vortices

The probabilities of exceeding the calculated peak suction were evaluated using the cumulative density function (CDF) of the measured pressure time series beneath the vortex cores, as shown in Table 6. Col 4 (Fig. 20) at a wind direction of 15° was taken as an example to illustrate the evaluation. Figs. 26(a) and 26(b) show the pressure time series of the vortex cores in Col 4 and its CDF curve. The calculated peak suction for the core of Col 4 was -3.192, whose exceeding probability was evaluated to be 0.3% according to the CDF curve in Fig. 26(b).

Fig. 25 indicates that calculated peak suction given by the improved model and Banks' model was always less than the measured values. Comparatively, the errors of the calculated results from the improved model were less than 13%, while those from Banks' model were less than 20%. This once again implies that Banks' model may underestimate the actual intensity of the conical vortices.

Comparing Figs. 25 and 21, the prediction accuracy of the mean suction beneath vortex cores was higher than that of the peak suction. This is due to the fact that the intense fluctuations induced by conical vortices increase the uncertainty of the pressure prediction and decrease the prediction accuracy. In the *China loading code for the design of building structures* (*GB50009-2001*), the peak factor (g) is proposed to calculate peak wind loads during the design of cladding and envelopes. The specified g is 2.2 in *GB50009-2001*, which represents a reliability of 98.61% and an exceeding probability of 1.39%. In Table 6, the exceeding probabilities of the calculated peak suction given by the improved flow model were less than 0.5% compared to the measured pressure time series beneath the vortex cores. It is noted that there are few instantaneous fluctuations larger than the predictions. Therefore, the peak suction calculated by the improved flow model could ensure the safety of large-span roofs exposed to conical vortices.

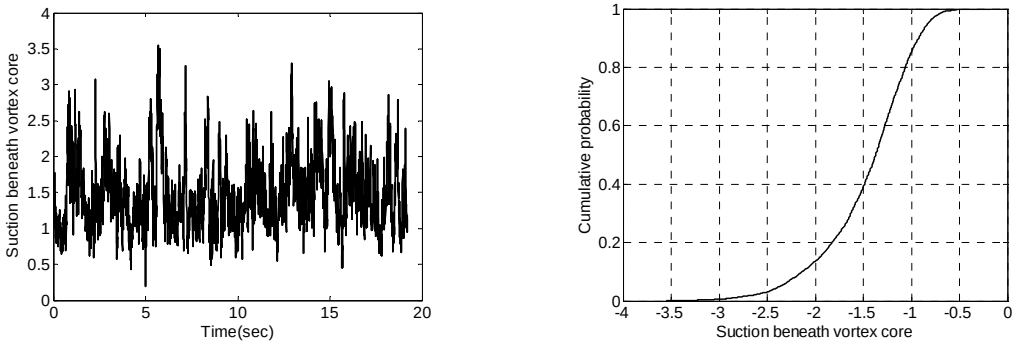

(a) Pressure time series beneath the vortex core (b) cumulative probability function

Fig. 26 Pressure time series beneath the vortex core and its cumulative probability function (Col 4, wind direction of 15°)

Table 6 Exceeding probabilities of calculated peak suction beneath the cores of the conical vortices

Wind direction	15°	30°	45°	60°	75°
Col 4	0.3%/ 0.68%*	0.28%/ 0.55%*	0.3%/ 0.5%*	0.03%/ 0.28%*	0.05%/ 0.32%*
Col 5	0.08%/ 0.27%*	0.02%/ 0.03%*	0.1%/ 0.25%*	0/ 0.16%*	0.03%/ 0.13%*
Col 6	0.12%/ 0.3%*	0.03%/ 0.05%*	0.05%/ 0.1%*	0.06%/ 0.2%*	0.08%/ 0.3%*
Col 7	0.3%/ 0.72%*	0.07%/ 0.07%*	0.1%/ 0.18%*	0.06%/ 0.25%*	0.13%/ 0.48%*
Col 8	0.62%/ 1.5%*	0.05%/ 0.2%*	0.1%/ 0.25%*	0.1%/ 0.36%*	0.12%/ 0.24%*
Col 9	0.38%/ 2.0%*	0.08%/ 0.2%*	0.2%/ 0.6%*	0/ 0.58%*	0.2%/ 0.58%*

Note: * represents the calculated results given by Banks' model

4.6 Application of the flow model to separation bubble

The improved flow model is also applicable to separation bubble, which is a two-dimensional vortex. The separation bubble is generated when the flow is normal to the leading edge. The pressures on the large-span roof at a wind direction of 90° (Fig. 15) were set as measured values for this portion of the study. The fitness of the flow model for predicting mean and peak suction beneath the cores of the separation bubble was verified by the measured results.

4.6.1 Prediction of mean suction beneath the cores of separation bubble

Eq. (23) is used to calculate the mean suction beneath the cores of the separation bubble. In Eq. (23):

- α =90° (normal to the leading edge);
- $\overline{U_T}/\overline{U_{ref}}$ =1.04 according to the fitting curve in Fig. 19;
- To evaluate the parameters of the separation bubble, conical vortices at a wind direction of 30°

(Table 4, vortex strength is 2.45) were used as a reference. The ratios $(U/U_T)^2$ and (R_c/h) belong to the separation bubble and the referenced conical vortices were analyzed. Based on these results, the ratio of intensity of the separation bubble to that of the referenced conical vortices was determined according to Eq. (19). It is clear from Table 3 that the integration in the vortex region (0.2<a<1) accounts for the largest percentage of vortex strength. Therefore, closer attention was paid to $(U/U_T)^2$ in the vortex region (0.2<a<1). In addition, the curvature radius of the streamlines in the separation bubble was difficult to calculate, so its influence was ignored. The ratio (R_c/h) was substituted with that of *h* (the height of the vortex core). To determine the ratios $(U/U_T)^2$ and *h*, the streamlines and colored charts showing the velocity in the separation bubble and the referenced conical vortices are illustrated in Fig. 27 using the PIV experiment.

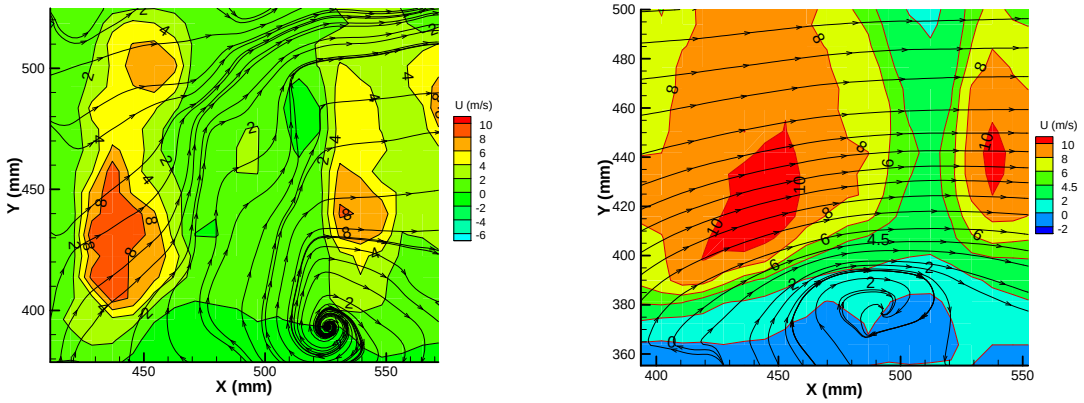

(a) Separation bubble (b) conical vortices (wind direction of 30°)

Fig. 27 Streamlines and colored charts showing the velocity in the separation bubble and conical vortices

Table 7 Parameters of the separation bubble and conical vortices

Parameters	$(U/U_T)^2$	h
Separation bubble	$(2/8)^2$	14 mm
Conical vortices (wind direction of 30°)	$(2/6)^2$	21 mm

The parameters of the separation bubble and the referenced conical vortices can be estimated from Fig. 27, as shown in Table 7.

Based on Table 7 and Eq. (19), the ratio of intensity for the separation bubble to that for the referenced conical vortices was calculated to be 0.375. According to Table 4, the intensity of the referenced conical vortices at a wind direction of 30° is 2.45, so the intensity of the separation bubble is 0.92, which is approximate to the proposed strength of 0.9 by Banks in the literature (Banks and Meroney, 2001). The mean suction beneath the cores of the separation bubble can then be calculated according to Eq. (23), for a result of $\overline{Cp_v} = -1.077$. (The intensity of the separation bubble was assumed to be uniform in the transverse direction, so the mean suction in the transverse direction was identical.).

The calculated $\overline{Cp_v} = -1.077$ was compared with the measured values to identify the effectiveness of the improved flow model. According to literature (Sun *et al.* 2009), the coverage area of the separation bubble on the large-span roof is approximately Y=155 mm (Fig. 28). Five sections normal to the leading edge were set as research objects within this range (Fig. 28: The section number is the number of the tap on the leading edge). The conditional sampling referenced in Section 4.4 was still used to calculate the pressure time series of the cores for different sections. The mean of the pressure time series was interpreted as the measured values of $\overline{Cp_v}$. Considering the symmetry of the flat roof, typical sections were only selected in the bottom half of the roof (Fig. 28). The comparison of the calculated $\overline{Cp_v} = -1.077$ and the measured $\overline{Cp_v}$ for different sections is given in Fig. 29. X represents the distance between the section and the bottom edge of the roof (Fig. 28). Because the intensity of the separation bubble given by Banks is close to the evaluated intensity in this study, the calculated results from Banks' model were not provided in this Section.

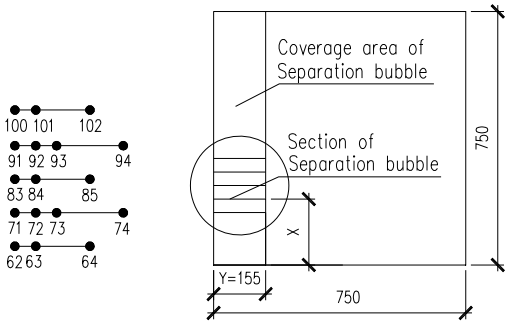

Fig. 28 Typical section of the separation bubble (unit: mm)

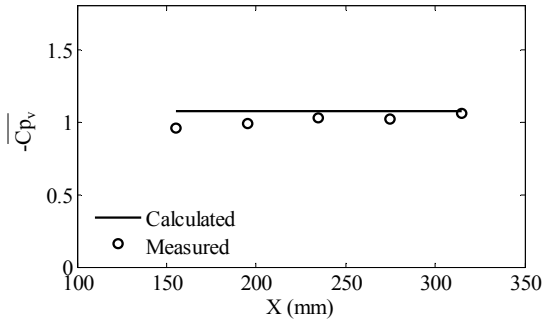

Fig. 29 Comparison of the calculated and measured mean suction beneath the cores of the separation bubble (wind direction of 90°)

Fig. 29 indicates that the calculated mean suction beneath the cores of the separation bubble is larger than the measured values. The errors of the calculated results were less than 13%, which indicates an adequate prediction. The evaluated intensity of 0.92 for the separation bubble on the large-span flat roof is reasonable.

4.6.2 Prediction of the peak suction beneath the cores of the separation bubble

The peak suction beneath the cores of the separation bubble were also calculated using Eq. (25), and the incident velocity is shown in Fig. 30. As mentioned in Section 4.5, the maximum of the pressure time series beneath the cores of the separation bubble (after conditional sampling) was taken as the measured value.

From Fig. 30, the ratio of maximum to mean velocity was calculated as $U_{ref\max}(t)/\overline{U_{ref}} = 1.57$, and the resulting $Cp_{v\max} = -2.655$ was calculated according to Eq. (25). Fig. 31 gives the comparison between the calculated and measured peak suction beneath the cores of the separation bubble.

Table 8 shows the exceeding probabilities of the calculated peak suction ($Cp_{v\max} = -2.655$), compared with the measured pressure time series of the cores. The evaluation is illustrated in Fig. 26.

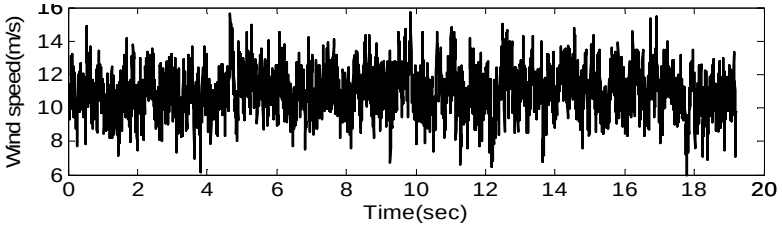

Fig. 30 Incident velocity at a wind direction of 90°

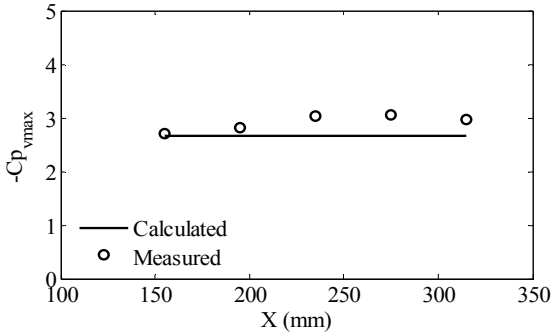

Fig. 31 Comparison of the calculated and measured peak suction beneath the cores of the separation bubble

Table 8 Exceeding probabilities of calculated peak suction beneath the cores of the separation bubble (wind direction of 90°)

Section	Col. 62	Col. 71	Col. 83	Col. 91	Col. 100
Exceeding probabilities	0.01%	0.03%	0.1%	0.1%	0.05%

Fig. 31 and Table 8 indicate that the errors of the calculated peak suction are less than 15%, with exceeding probabilities of less than 0.1%. In addition, the calculated peak suction was less than the measured values. This is due to the fact that the non-Gaussian pressure fluctuations under the separation bubble lead to erratic large spikes in the pressure time series. However, the exceeding probabilities in Table 8 imply that fluctuations beyond the predictions are rare. With a higher reliability, the calculated peak suction could ensure the safety of large-span roofs. Therefore, the improved flow model can not only apply to the prediction of suction beneath conical vortices, but it is also appropriate for predicting suction beneath separation bubble on large-span roofs.

Research has indicated that the quasi-steady theory underestimates the actual peak suction in the flow separation region (Banks *et al*. 2000), which is due to the quasi-steady theory assuming that pressure fluctuations on roofs are generated by the fluctuating component in the incident flow, while the crucial effect of vortices on pressure fluctuations is ignored. The flow model in this study establishes a relationship between the incident flow, the vortex and the roof suction. Based on this model, the peak suction beneath conical vortices and separation bubble were calculated, and these calculations' errors and exceeding probabilities were kept within a reasonable range.

5. Conclusions

Through a PIV experiment, the existence of separation bubble and conical vortices on a large-span flat roof was verified. A two-dimensional flow model of conical vortices was improved and validated based on the measured velocities in vortices. According to this flow model, the intensities of the conical vortices under different wind directions were given. The main conclusions of this work can be summarized as follows:

- When the flow is normal to the leading edge, separation bubble occurred on the large-span flat roof. Negative vorticity is distributed around the separation bubble, with

their peak corresponding to the vortex core. The magnitude of the negative vorticity decreases downstream. Under a cornering flow, conical vortices are observed near the leading edge of the flat roof. The appearance of conical vortices is influenced by the wind angle. When the wind changes from running along the diagonal to deviating from the diagonal of the roof, the conical vortex close to the approaching flow changes from a circular into a more oblong shape. The peak negative vorticity is then located near the leading edge and around the vortices. Positive vorticity is distributed uniformly above the conical vortices.

- The vortex can be seen as an amplifier that amplifies and transfers pressure above the vortex to the roof surface. This amplification factor demonstrates the intensity of the vortices. The curvature radius of the streamlines in the vortices and the rotational velocity of the vortices are confirmed to have an influence on the vortex strength. A larger curvature and faster rotational speed cause greater suction beneath the vortices, with the latter former playing a more important role.
- The mean suction beneath the cores of the conical vortices was calculated using both the improved model and Banks' model. The results indicate that the calculated suction given by the improved model in this study is larger than that from Banks' model. Compared with the measured values, the errors of the mean suction from the improved model are less than 10%, while those from Banks' model are less than 15%. Therefore, the flow model of this study is more accurate in predicting mean suction beneath the cores of conical vortices.
- The quasi-steady theory was corrected by considering the effect of vortices on generating pressure fluctuations. Based on this idea, the improved model and Banks' model were employed to predict peak suction beneath the cores of the conical vortices. Compared with the measured values, the errors of the peak suction given by the improved model are less than 13%, and the exceeding probabilities are less than 0.5%, while errors of the calculated results from Banks' model are less than 20%, with the exceeding probabilities less than 1%. Therefore, the improved model predicted peak suction with higher reliability could ensure the safety of large-span roofs exposed to conical vortices.
- The intensity of the separation bubble on the large-span roof is evaluated using the measured velocities and height of the vortex core. Based on this procedure, the mean and peak suction beneath the cores of the separation bubble were predicted using the improved model. Compared with the measured values, the errors in the calculated mean suction are less than 13%, while errors in the peak suction are less than 15%, with exceeding probabilities of less than 0.1%. Consequently, the improved flow model can also apply to the prediction of suction beneath the cores of separation bubble.

Acknowledgements

The essential contributions of Prof Chen Zhengqing, Associated Prof. Hua Xugang and Teacher Niu Huawei in arranging and coordinating the PIV experiment are gratefully acknowledged. Postgraduate students Zuo Taihui, Zhang Qinglin, Hu Pengjun, Bao Huanhuan, Chen Hailong and Hua Wenlong contributed greatly in assisting on the PIV experiment. This work is supported by the National Science Foundation for Distinguished Young Scholars of China (Grant No. 51125031).

References

Banks, D. (2000), *The suction induced by conical vortices on low-buildings with flat roofs*, Ph.D. dissertation, Civil Engineering, Colorado State University, Fort Collins, Colorado.

Banks, D., Meroney, R.N., Sarkar, P. P. , Zhao, Z. and Wu, F. (2000), "Flow visualization of conical vortices on flat roofs with simultaneous surface pressure measurement", *J. Wind Eng. Ind. Aerod.*, **84**, 65-85.

Banks, D. and Meroney, R.N. (2001a), " A model of roof top surface pressures produced by conical vortices: Evaluation and implications", *Wind Struct.*, **4**(2), 1-20.

Banks, D. and Meroney, R.N. (2001b), "A model of roof-top surface pressures produced by conical vortices: model development",*Wind Struct.*, **4**(3), 227-246.

Banks, D. and Meroney, R.N. (2001c), "The applicability of quasi-steady theory to pressure statistics beneath roof-top vortices", *J. Wind Eng. Ind. Aerod.*, **89**, 569-598.

Cook, N.J. (1985), *The designer's guide to wind loading of building structures*, part1, Building Research Establishment, Garston, UK.

Ekaterinaris, J.A. and Schiff, L.B. (1994), " Numerical simulation of incidence and sweep effects on delta wing vortex breakdown", *J. Aircraft*, **31**(5), 1043-1049.

Gioffre, V.G. and Grigoriu, M. (2001), "Non-Gaussian wind pressure on prismatic buildings. II: numerical simulation", *J. Struct. Eng. - ASCE* , **127**(9), 990-995.

Kasperski, M., Koss, H. and Sahlmen, J. (1996) , "BEATRICE Joint Project: Wind action on low-rise buildings: Part1. Basic information and first results", *J. Wind Eng. Ind. Aerod.*, **64**, 101-125.

Kawai, H. and Nishimura, G. (1996), "Characteristics of fluctuating suction and conical vortices on a flat roof in oblique flow", *J. Wind Eng. Ind. Aerod.*, **60**, 211-225.

Kawai, H. (1997), "Structure of conical vortices related with suction fluctuation on a flat roof in oblique smooth and turbulent flow", *J. Wind Eng. Ind. Aerod.*,**69-71**, 579-588.

Kawai, H. (2002), "Local peak pressure and conical vortex on building", *J. Wind Eng. Ind. Aerod.*, **90**, 251-263.

Kim, K.C., Ji, H.S. and Seong, S.H. (2001), "PIV measurement of roof corner vortices", *Wind Struct.*, **4**(5), 441-454.

Lin, J.X., Surry, D. and Tieleman, H.W. (1995), "The distribution of pressure near roof corners of flat roof low buildings", *J . Wind Eng. Ind. Aerod.*, **56**, 235-265.

Lin, J., Ruan, X. and Chen, B. (2005), *Fluid mechanics*, Tsinghua University Press, Beijing, China. (in Chinese)

Marwood, R. and Wood, C.J. (1997), "Conical vortex movement and its effect on roof pressures", *J. Wind Eng. Ind. Aerod.*, 69-71, 589-595.

Rizzi, A. and Muller, B. (1989), "Large-scale viscous simulation of laminar vortex flow over a delta wing", *AIAA J.*, **27**(7), 833-840.

Simiu, E. and Scanlan, R.H. (1996), *Wind effects on structures*: *an introduction to wind engineering*, 3rd Ed., A Wiley-Interscience Publication, New York.

Sun, Y., Zhao, B. and Cao, Z. (2009), "Comparison of shape factors for flat and domed roofs in different countries wind load standards", *Spatial Structures*, **15**(2), 16-21. (in Chinese).

Tieleman, H.W., Surry, D. and Mehta, K.C. (1996), "Full/model-scale comparison of surface pressures on the Texas Tech experimental building", *J. Wind Eng. Ind. Aerod.*, **61**, 1-23.

Tryggeson, H. and Lyberg, M.D. (2010), "Stationary vortices attached on flat roofs", *J. Wind Eng. Ind. Aerod.*, **98**, 47-54.

Wu, F., Sarkar, P.P., Metha, K.C. and Zhao, Z. (2001), "Influence of incident wind turbulence on pressure fluctuations near flat-roof corners", *J. Wind Eng. Ind. Aerod.*, **89**, 403-420.

Xu, H. (1987), *Basis for aerodynamics*, Beijing Aviation College Press, 62-64. (in Chinese).

Zhao, Z. (1997), *Wind flow characteristics and their effects in low-rise buildings*, Ph.D. dissertation, Civil Engineering, Texas Tech University, Lubbock, Texas.

JH